ELSEVIER

Polymer 41 (2000) 4291–4307

polymer

Compressive stress–strain properties of automotive paints over a range of strain rates and temperatures

I. Rumzan, J.G. Williams*

Department of Mechanical Engineering, Imperial College of Science, Technology and Medicine, Exhibition Road, London SW7 2BX, UK

Received 4 March 1999; received in revised form 9 June 1999; accepted 5 July 1999

Abstract

In this paper, the compressive stress–strain properties of automotive paints referred to as coatings A_1, A_2, A_3, B, C and D are presented over a range of strain rates of 10^{-3}–10^4 s^{-1} and temperatures of −20, 0, 20 and 40°C. From these results, the 10% flow stress is plotted against the log (strain rate) using temperature dependent shift factors that can combine results at all temperatures and obtain *master* curves for each coating. This also includes a mapping of chipped, cracked and unfailed specimens during testing.

Keywords: Compressive stress–strain properties; Temperature dependent shift factors; Strain rates

1. Introduction

In the past decade, the processes involving the manufacturing and application of automotive paints or coatings have undergone changes because of new legislation and considerations of energy conservation, environmental control and consumer demands. The latter is an important factor in that guarantees of 3–5 years against cosmetic damage and 5–10 years against corrosion are targets for companies. Indeed, this is the main motivation behind obtaining an automotive paint system that will, in most cases, not suffer any serious damage before the guaranteed period. Corrosion of the substrate induced by chipping and cracking of the paint due to stone impact has made the design against corrosion and cosmetic damage a harder task. Although many experimental tests have been performed that try to reproduce the stone impact in the laboratory, the results have been too crude to have any serious effect at the design stage. In addition, the numerical work done in that direction has been too simplified to give any proper understanding of the problem.

In this paper, a more fundamental approach is described and involves the determination of the stress–strain properties of the paint layers over a range of strain rates (specially at high rates) and temperatures (for variations in weather conditions), since the automotive paints are essentially a set of highly engineered thin polymer coatings adhering to each other and to the substrate (steel or plastic) as shown in Fig. 1. A description of the experimental apparatus used to test these coatings at different strain rates and temperatures is given together with a method of verifying the accuracy of the results in terms of the assumptions made to deduce the stresses and strains. Furthermore, with a view in achieving the ultimate goal, which is the impact resistance of the paints, it is illustrated how plots of the 10% flow stress against strain rate may be made using temperature dependent shift factors. This facilitates the inclusion of results at other temperatures on the same curve and yields an empirical prediction of the safe and unsafe regions (with strain rate and temperatures) in terms of chipping and cracking of paint specimens. It also facilitates the extrapolation of data to higher strain rates.

1.1. Materials used

Coatings A_1, A_2 and A_3 are clearcoats that consist mainly of acrylic resins and melamine resins as binders and additives mostly of a UV-absorber and a radical scavenger. Coating B is a solvent-borne basecoat, which is made of a binder of resin systems containing polymers and amino melamine resins crosslinked with alkydes. Coating C is a primer coating consisting mainly of the binder, which in most cases, is hydroxy functional saturated polyester crosslinked with melamine formaldehyde and sometimes isocyanates and benzoguanamine resins. Coating D is a multi-layer coating consisting of A_1, B and C.

* Corresponding author.

0032-3861/00/$ - see front matter
PII: S0032-3861(99)00499-1

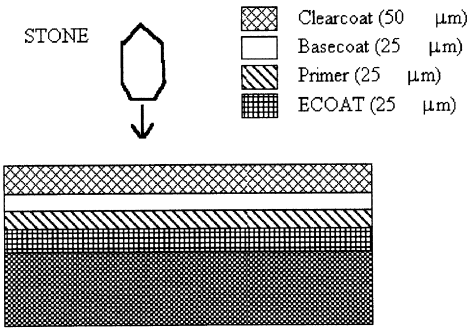

Fig. 1. Multiple layer paint systems.

2. Experimental apparatus

2.1. Introduction

The experimental procedure used here to obtain stress–strain data for materials over a range of strain rates was developed by Dioh [1]. In his work, he presented stress–strain results over a range of strain rates of 10^{-4}–10^{3} s^{-1} and temperatures of -20 to 40°C.

2.2. Preparation of specimens

Automotive paint preparation is very complex, and the mechanical properties of the films are very much dependent on their thickness as well as other factors such as curing time and temperature which are all closely related to the preparation. The materials were prepared as coatings that were peeled from the tedlar film substrate to give films of approximate thickness of 25–50 μm. The specimens were prepared by using a stainless steel tool punch (Fig. 2) with a manual punch set to make circular discs of the required diameter which were then stacked together to make up the required thickness. This method proved to be less time consuming than the method used by Dioh [2], but its accuracy depends on how well the punch tool was machined. The main uncertainty with stacking paint films lies in the fact that the adjacent films are held together during testing by compression only, and the boundary conditions at these interfaces are unknown.

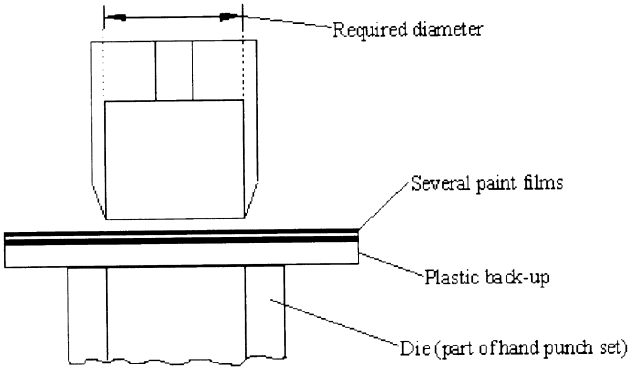

Fig. 2. Punch for making.

The ideal situation would be to have an apparatus that could test a single paint film but this is not practical because the friction at the metal/specimen interface would have too much influence on the conditions inside the specimen.

2.3. High strain rates: split Hopkinson pressure bar

A schematic diagram of the bar system is shown in Fig. 3. The function of the momentum bar is to take the momentum of the impact away so that the transmitted strain pulse is not reflected back at the end of the transmitter bar.

The vacuum air gun consists of a 2.3 m long steel barrel having a polished internal bore of diameter 63.5 mm, and is connected at its two ends to a pump. The projectile speed is varied by orifice plates that alter the rate of air entry which accelerate the projectile after a vacuum has been created in the gun. Six infrared emitter/receiver pairs in brass mounts at the firing end of the gun were used initially to calibrate the orifice plates to 10,15, 20 and 25 ms^{-1}. The projectile is a bar of the same material and diameter as the incident and transmitter bars and is housed in a cotton reel shaped PTFE guide. Its length is either 200 or 300 mm depending on the time duration of the stress pulse that is required (usually approximately 100 μs).

The bars are all 15.8 mm in diameter (5/8 in.) and are made of a high strength aluminium HE15, with a yield stress of approximately 410 MPa, a modulus of 73.1 GPa and a density of 2796 Kg m^{-3}. The ends of the bars where the specimen is located are accurately ground and polished in situ to obtain smooth parallel faces between which the specimen is compressed. The gas gun rests on a rigid steel support that keeps it aligned horizontally and minimises vibration. The split Hopkinson pressure bar (SHPB) bars are held on separate supports (no vibration transmission) which are V-shaped nylon clamps that can be accurately adjusted in the vertical direction by a screw and in the other two directions manually. Small rubber pads are placed in between the nylon clamps and the bars before tightening the supports in order to minimise any spurious reflections.

The strain gauges were located on the surface of the bars, 400 mm on each side of the specimen and were mounted in pairs diametrically opposite on the surface of the bars to remove any effects of bending waves. The resistance and gauge factors of the gauges are 120 Ω and 2.06, respectively. Each pair of gauges (one on the incident bar and one on the transmitter bar) were wired in series to give a total resistance of 240 Ω and form one arm of a Wheatstone bridge in the FYLDE 359TA strain gauge amplifier (a gain of 100 was used), incorporating three 240 Ω resistors. The amplified strain gauge signals were then recorded in the 1 MHz digitizer board of the Nicolet 500 data acquisition unit. The unit has four channels while either two or three are needed. Two channels are used for each pair of strain gauges, and the third channel can be connected to the velocity measuring system to use this signal as trigger. Alternatively, the signal from the incident strain pulse can

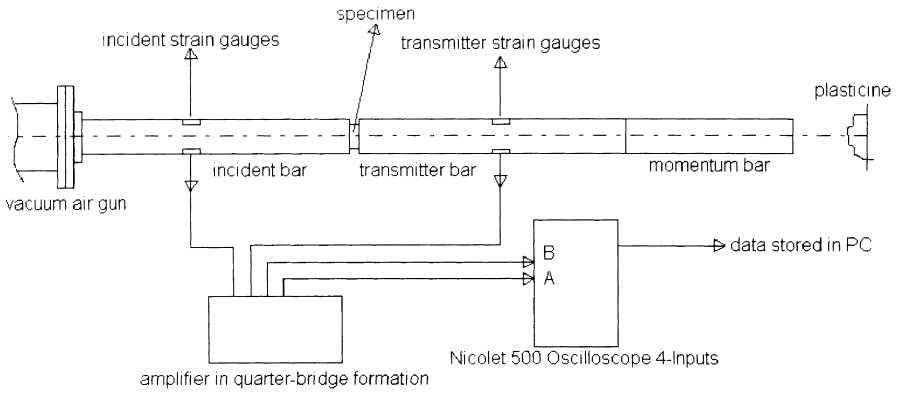

Fig. 3. A schematic diagram of the SHPB experimental set-up.

be used as a pre-trigger. This data is then captured into a microcomputer where it is stored for processing. The strain $\varepsilon(t)$ (function of time) is calculated from the voltage measurement $v(t)$ (function of time) by Eq. (1).

$$\varepsilon(t) = \frac{4v(t)}{V_s F G} \tag{1}$$

where V_s is the supply voltage of amplifier, F the gauge factor of strain gauge and G the amplifier gain.

The reflected (obtained from the gauge on the incident bar) and transmitted (gauge on the transmitter bar) strain pulses (ε_R and ε_T) needed for the analysis, are firstly smoothed to remove any dispersion and noise effects. They are processed automatically using a commercial software FAMOS on which a sequence is written which uses Kolsky's analysis [3] namely Eqs. (2)–(4) to calculate the stress, strain and strain rate as a function of time in the specimen.

$$\varepsilon_S = \frac{-2C_0}{L}\int_0^t \varepsilon_R \, dt \tag{2}$$

$$\sigma_S = \frac{F}{A_S} = E\frac{A}{A_S}\varepsilon_T \tag{3}$$

$$\dot{\varepsilon}_S = \frac{-2C_0}{L}\varepsilon_R \tag{4}$$

where ε_S, $\dot{\varepsilon}_S$, σ_S are the strain, strain rate and stress in the specimen, respectively. The true stress σ_t and true strain ε_t are then obtained from equations:

$$\varepsilon_t = \ln(1 + \varepsilon_S) \qquad \sigma_t = \sigma_S(1 + \varepsilon_S)$$

This sequence also matches the start of the reflected and transmitted strain pulses in time and the stress–strain curve is then obtained by combining σ_t with ε_t. The

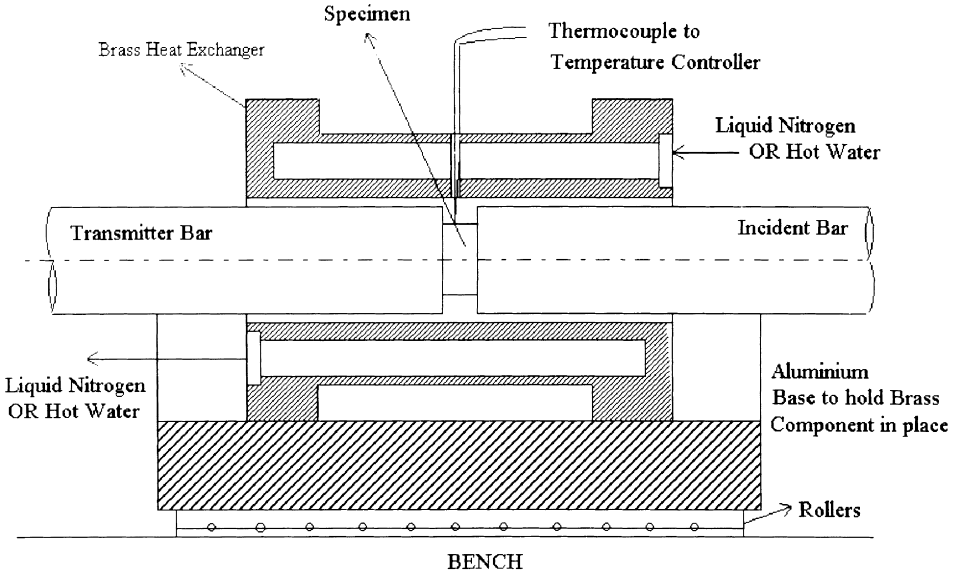

Fig. 4. Rig for SHPB tests at different temperatures.

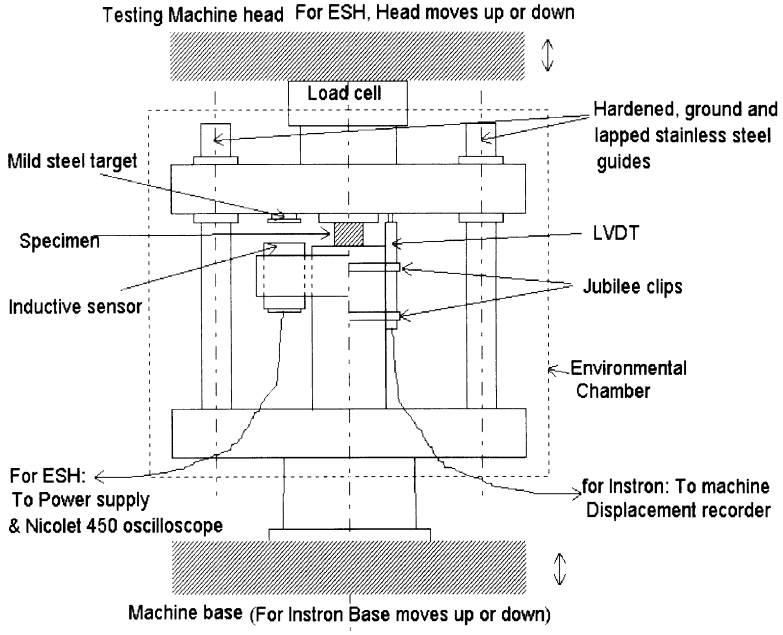

Fig. 5. Rig for low and Intermediate rate tests.

specimen used is 12.7 mm in diameter and 1.5 mm in thickness for most tests. Vaseline was used as a lubricant

The arrangement shown in Fig. 4 was used to perform tests at different temperatures namely −20, 0 and 40°C. For low temperatures (−20, 0°C), liquid nitrogen is circulated through the brass heat exchanger while for high temperatures (40°C), hot water is used. The thermocouple is a welded-tip PTFE insulated K-type with a range of −50 to 200°C, and is inserted as close as possible to the specimen.

For low temperatures, a CAL9900 temperature controller controls the temperature of the specimen via a feedback loop with the thermocouple, and this is done through an ALCAN solenoid valve attached to the outlet of the liquid nitrogen tank. For high temperatures, the system used for providing hot water has an in-built system for controlling its outlet temperature.

2.4. Low and intermediate strain rate tests

Low strain rate tests (10^{-4}–10^{-2} s^{-1}) were carried out on a screw driven Instron mechanical testing machine and Intermediate strain rate tests (10^{-1}–10 s^{-1}) were performed on an ESH servo-hydraulic testing machine. In both cases, the load is applied via a specially designed compression tool.

Fig. 5 shows the arrangement used in all the tests. The test procedure is in accordance with ASTM standard D695-89 for determining the compressive properties of rigid plastics. The compression tool provides precision axial loading of the specimen applied through surfaces which can be carefully ground and polished. Hence, any misalignment in the radial direction is reduced. Different rates are obtained from different crosshead speeds of the machine and they were calibrated according to the manufacturer's specifications before they are used.

A linear voltage displacement transducer (LVDT) was used to measure the axial displacement of the specimen (which was 4.4 mm in thickness and 12.7 mm in diameter) instead of the in-built displacement measurement system based on the crosshead. This ensures that the true axial displacement of the specimen is recorded. For tests on the ESH machine, inductive sensors were preferred to the LVDT since they have a faster response. Two sensors were used initially on opposite sides of the specimen to check whether there was any misalignment in the sensor placement. The load is monitored via the machine load cell and the load-displacement data is recorded automatically in a microcomputer connected to the machine. For the ESH machine tests, the Nicolet 450 was used to record the data and store it. The stress and strain can then be calculated since the geometry of the specimen is known. For tests at room temperature and higher, candle wax was used as lubricant but for lower temperature tests, the wax was too hard and vaseline was used. The temperature of the tests can be varied by using the environmental chamber of the machine and the same range as before was used.

3. Verification of results

3.1. Validation of low and intermediate strain rate tests

3.1.1. Repeatability

All tests are repeated and the load-displacement curves were compared. Initially, significant scatter was obtained which was due to the multiple layers constituting the

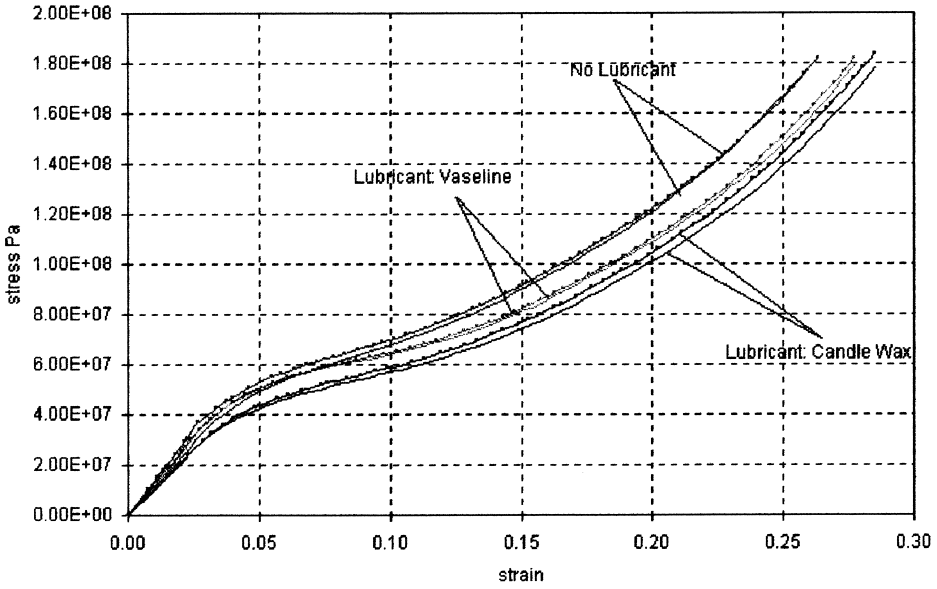

Fig. 6. Coating C Instron test rate 0.0044 s^{-1} (compare lubricants).

specimen not being stacked together as one material when the load was applied. In order to remove this, the specimen was pre-compressed to a certain load, the value of which depended on the yield load for the low strain rate regime determined from a first preliminary test: the pre-compressed load was then taken as 10% of the yield load (varying between 0.5 and 1.5 kN depending on the coating).

3.1.2. Validity of assumptions used

The main factor that can affect the assumption of uni-axial compression is friction at the interface between the specimen and the metal comprising the rig (EN24 steel on top and carbon steel at the bottom). Three different states at the interfaces were investigated: lubricated with vaseline; lubricated with candle wax; and no lubricant. As shown in Fig. 6, there is a definite discrepancy in the results, even between the two different lubricants. Since a higher friction state will cause higher stresses/loads for the same strains/displacements, it is clear that candle wax is a better lubricant than vaseline for these tests.

Friction effects will only be significant if the specimen diameter/length ratio d/l is large i.e. the specimen is thin compared to its diameter. In our tests,$d/l = 2.9$. Ideally, for no friction, the specimen should be infinitely long, i.e. $d/l = 0$. In order to investigate these geometry effects, tests were performed at the same strain rate of 0.01 s^{-1} on coating C for $d/l = 12.9$, 6.24 and 3.15 (Speeds of 0.5, 1.0 and 2.0 mm min^{-1}, respectively).

In Fig. 7, the stress at 5,10 and 15% strain is plotted against d/l, and as it can be seen, a stress increase only starts to be apparent for $d/l = 10$ or higher. Between 0 and 6, the

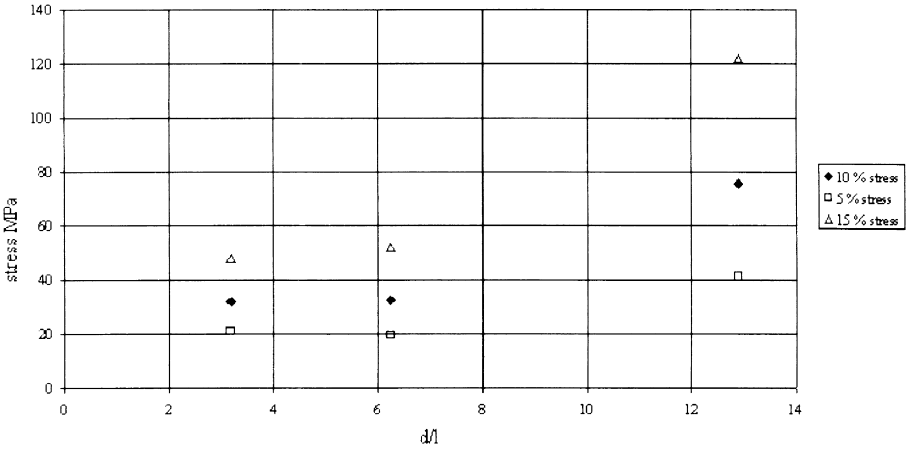

Fig. 7. Coating C d/l variation strain rate = 0.01 s^{-1}.

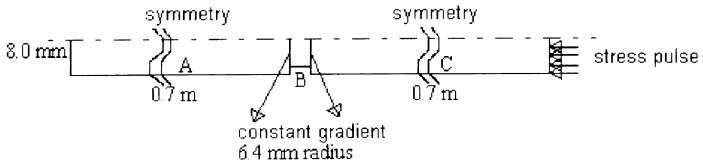

Fig. 8. An FV model of SHPB.

stress is fairly constant indicating a small friction effect. As for our tests, $d/l = 2.9$, we can say the effect of friction is negligible.

3.2. Validity of high strain rate results

3.2.1. Introduction

The tests were repeated for each speed and good agreement was obtained. A thorough investigation of friction and geometry effects was not thought to be worthwhile since the results were corrected by using a finite volume simulation of the SHPB with Kolsky's first approximation of the stress–strain curve as an elastic–plastic material model of the specimen. Such a process was found to be very important, although time consuming and computer intensive, as discrepancies in the stress pulses from the simulation and the experiment of up to 25% were obtained for most curves.

3.2.2. Finite volume model of SHPB

The SHPB was modelled in 2D (axisymmetric), and it was made up of both the aluminium bars and the specimen, as shown in Fig. 8. The model has five elements along B and 957 elements along each of A and C. In terms of time step size, from equation

$$\delta t_{\max} = \frac{\delta x_{\min}}{C_{b\max}}$$

with $\delta x_{\min} = 0.3$ mm and $C_{E\max} = 5113\ \mathrm{ms}^{-1}$ (aluminium), i.e. $\delta t_{\max} = 5.86 \times 10^{-8}$ s.

We use eight elements along the bar radius and six elements along the specimen radius (gives an element radius of 1.0 mm).

In terms of boundary conditions, symmetry is applied at the centre and the other surfaces are made free. At the impact side of the input bar, a stress pulse is applied. The rise time, fall time, pulse length and stress magnitude is obtained from the input pulse in the experiment. In order to compare the simulation with the experimental data from the strain gauges, the stress pulses (on the bars at distances of 0.4 m from each side of the specimen: at the same position where the strain gauges were placed in the experiment) were extracted from the simulation. Furthermore, the average strain rate and the average strain in the specimen were stored as a function of time. For the material model, the aluminium bars are modelled as a linear elastic material with an elastic modulus of 73.1 GPa and a density of 2796 kg m^{-3}. The density of the paint is taken as 1200 kg m^{-3}.

3.2.3. Comparison with experimental data

1. Initially, the nominal stress–strain curve from Kolsky's analysis is used as the material property of the specimen (elastic–plastic model), and the following method is

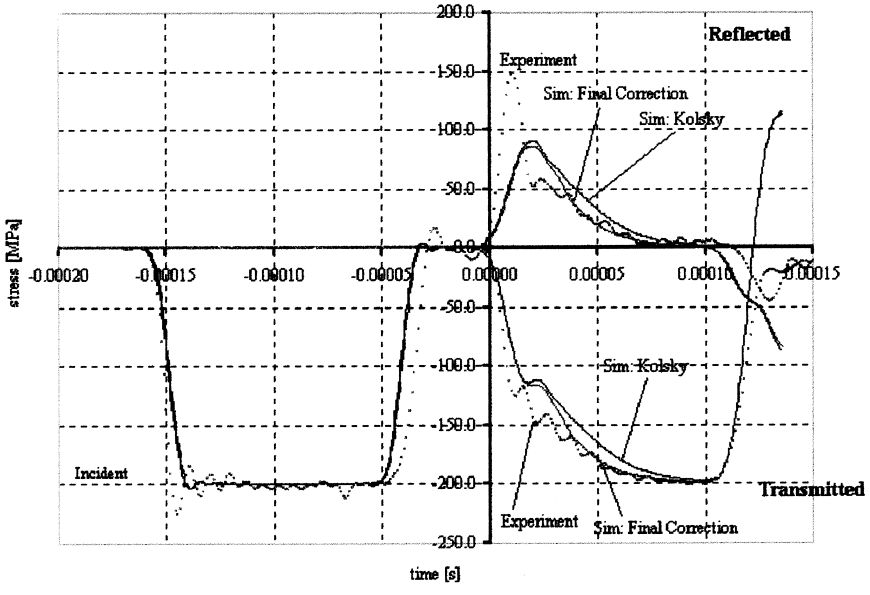

Fig. 9. Comparison between experimental and simulated stress pulses for Coating C.

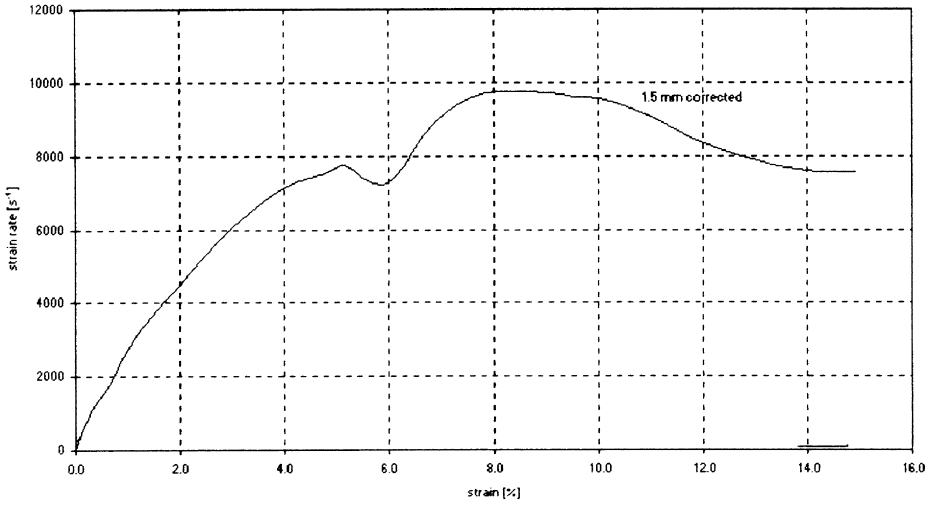

Fig. 10. Comparison of strain rate versus strain in specimen.

adopted to assess whether this curve needs correction or not:

2. Find the average percentage difference Δ between the transmitted experimental and numerical stress pulses in terms of the difference in the stress magnitudes. This is done since the stress values in the transmitted pulse are proportional to the stress values in the specimen based on Kolsky equation (3).
3. If $\Delta > 8\%$, the nominal stress–strain curve is then corrected by adding Δ to all the stress values as given below

$$\sigma_{se}^{new} = \frac{\Delta\sigma_{se}^{old}}{100} + \sigma_{se}^{old}$$

where σ_{se} is the nominal stress value of stress − strain curve.

4. The gradient of the plastic part of the transmitted pulses is also compared. The average gradient of a transmitted pulse is given by

$$\alpha = \frac{1}{m}\sum_{t=t_p}^{t_2} \frac{\sigma_t - \sigma_{t-\delta t}}{\varepsilon_t - \varepsilon_{t-\delta t}}$$

where t_p is the time start of plastic part of transmitted pulse and m the number of points between t_p and t_2. Then, the average gradient of the new nominal stress–strain curve is given by

$$\alpha_{se}^{new} = \frac{\alpha_{num}}{\alpha_{exp}} \times \alpha_{se}^{old}$$

5. The nominal stress–strain curve is then corrected by modifying the plastic stresses σ_{se}^{new} using the difference between σ_{se}^{new} and α_{se}^{old}.

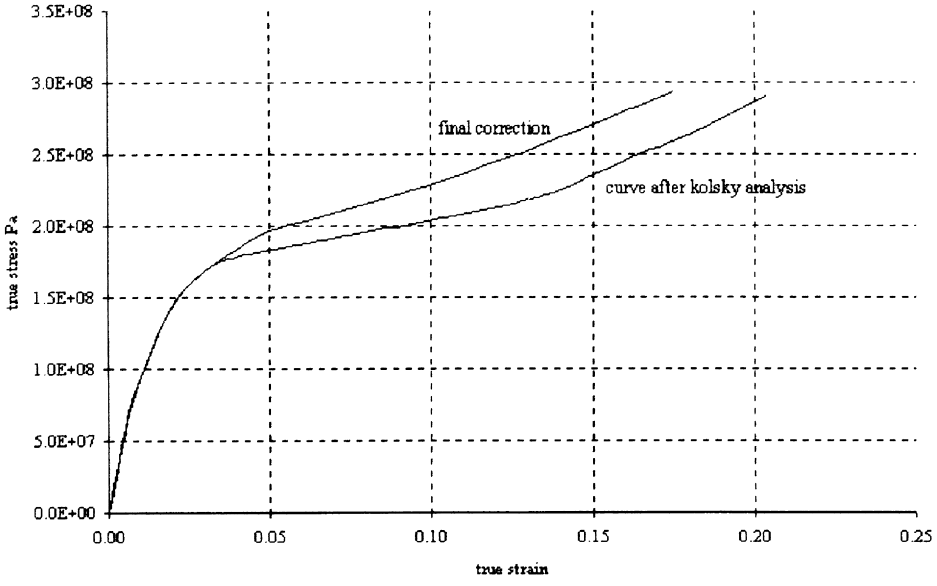

Fig. 11. Corrected true stress–strain curves for Coating C.

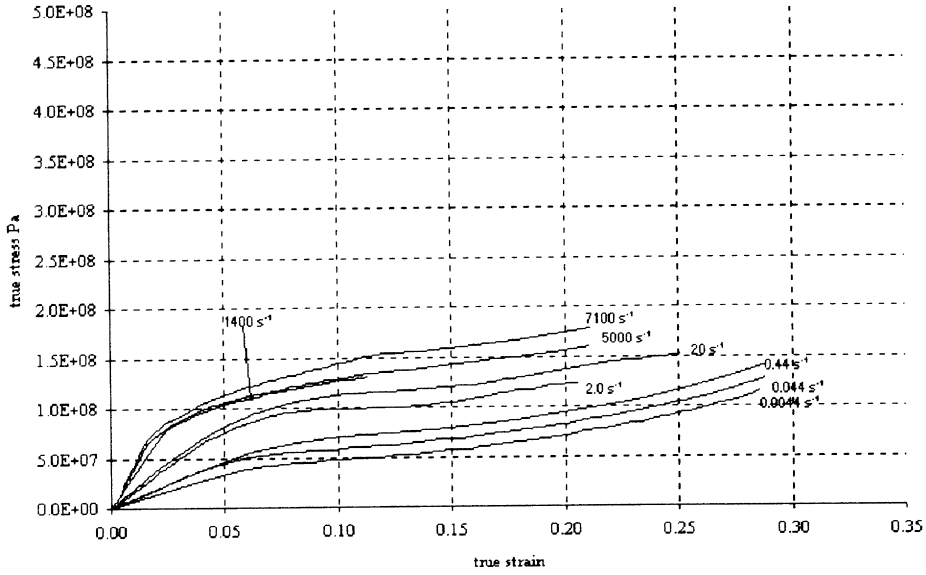

Fig. 12. Coating A_1: true stress–strain variation with strain rate at 20°C.

$$\sigma_{\mathrm{Pse}}^{\mathrm{new}} = (\varepsilon_{\mathrm{se}}^{\mathrm{old}} - \varepsilon_{y}^{\mathrm{old}})(\alpha_{\mathrm{se}}^{\mathrm{new}} - \alpha_{\mathrm{se}}^{\mathrm{old}}) + \sigma_{\mathrm{Pse}}^{\mathrm{old}}$$

where $\sigma_{\mathrm{se}}^{\mathrm{old}}$ is the plastic stresses at corresponding strains in old se-curve.

This is done by writing a FORTRAN subroutine and an example of the comparison process is given below.

As shown in Fig. 9 for Coating C at 0°C, a marked discrepancy ($\Delta = 13\%$) between the experimental and simulated transmitted stress pulse obtained when the Kolsky stress strain curve was used as material property for the specimen. By using the comparison method described above, two iterations brought the difference Δ down to 6% as shown by the 'final corrected pulse' in Fig. 9; if more iterations were performed, a negligible change in Δ was obtained (this was thought to be due to limitations in the accuracy of the model in terms of mesh size and proper boundary condition modelling at the specimen/bar interfaces) but it was accurate enough in terms of the correction from Kolsky's analysis.

The average strain rate versus average strain in the specimen (Fig. 10) for the specimen during the final iteration gives the average strain rate in the specimen (averaged between 5 and 15% strain, $\dot{\varepsilon} = 8000\ \mathrm{s}^{-1}$) and the difference between the final corrected true stress–strain curve and the original Kolsky true stress–strain curve is given in Fig. 11.

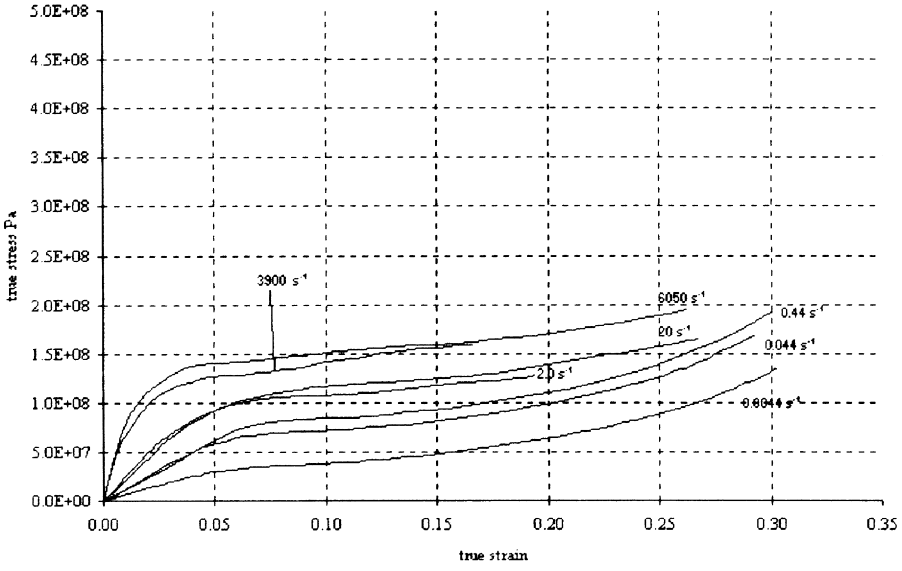

Fig. 13. Coating A_2: true stress–strain variation with strain rate at 20°C.

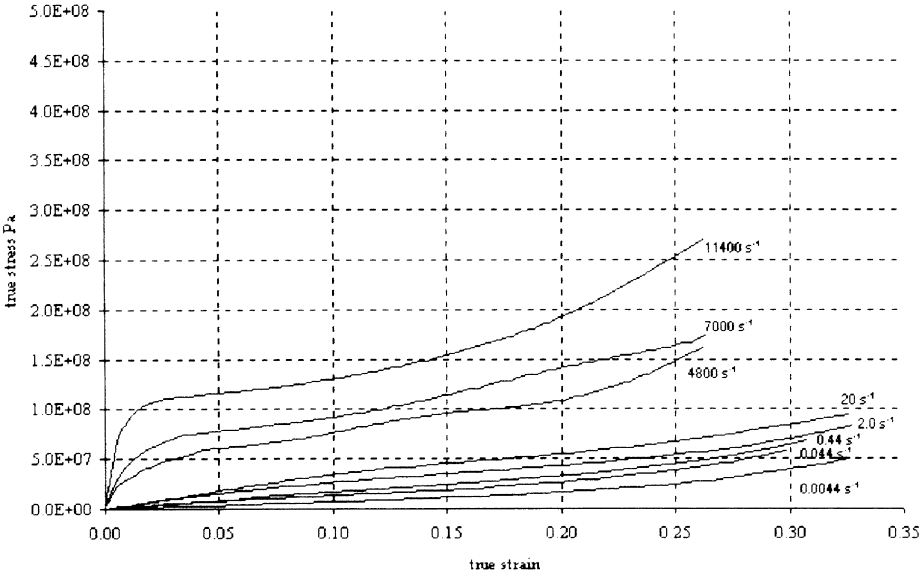

Fig. 14. Coating A_3: true stress–strain variation with strain rate at 20°C.

4. Results and discussion

4.1. Compressive stress–strain curves

The experimental results of each paint material are spread over a wide range of temperatures and strain rates, and it is therefore necessary to organise these data in an orderly manner so that sensible conclusions about the material behaviour are obtained. In this paper, the true stress–strain curves are compared with respect to strain rate and material type, and this is done systematically by using the following parameters: elastic modulus; strain hardening factor; and stress levels.

4.1.1. Comparison at different strain rates

The true stress–strain curves at room temperature and all strain rates for each coating are presented in Figs. 12–17. At most temperatures, the amount of strain hardening is constant with strain rate except for a few cases. For Coating A_1 (Fig. 12), the strain hardening increases at $\dot{\varepsilon} > 8 \times 10^3\ s^{-1}$ and $\varepsilon > 20\%$.

For Coating A_3 (Fig. 14), there is an increase in strain hardening for $\dot{\varepsilon} > 10^4\ s^{-1}$ and $\varepsilon > 20\%$, and for Coating D (Fig. 17), the strain hardening increase occurs for $\varepsilon > 16\%$ and the same strain rate.

4.1.2. Strain rate softening behaviour

In general, the materials show a continuous stress increase with strain rate, but this is not the case for Coating B at 20 and 40°C (Figs. 15 and 19) and for Coating A_3 (Fig. 18) and Coating D (Fig. 20) at 40°C where the stress strain

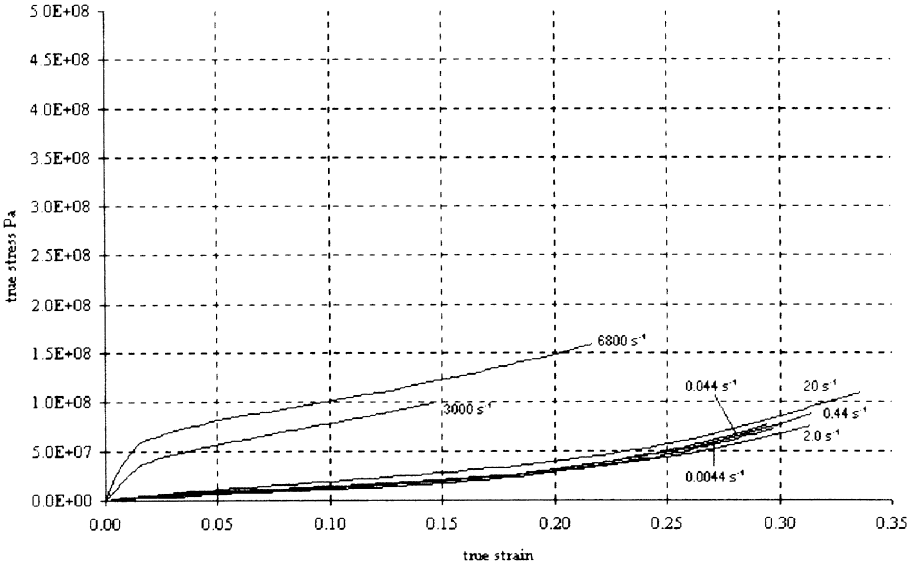

Fig. 15. Coating B: true stress–strain variation with strain rate at 20°C.

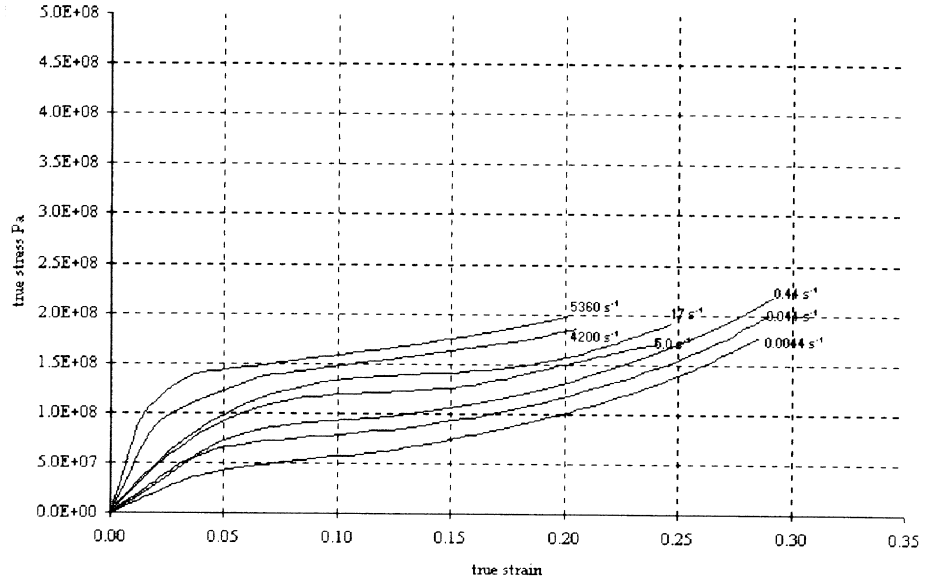

Fig. 16. Coating C: true stress–strain variation with strain rate at 20°C.

curves at intermediate strain rates have lower stress values than those at low strain rates. Strain rate softening normally occurs due to adiabatic heating at higher strain rates [4] but at even higher strain rates, the strain hardening factor due to strain rate is dominant. In Section 4.2, where the strain rate and temperature behaviour of the paints are compared to Eyring theory [5] and a method of reduced variables [6], it could be seen that the fact that strain rate softening only acts for the above-mentioned three materials could be related to the two-process Eyring theory described later. However, the fact that the difference between the curves is quite close, could also be an effect of random error. Hence, only a serious statistical analysis will be able to confirm this strain rate softening effect. (This is beyond the scope of this paper.)

4.1.3. Comparison between different materials at high rate

In Fig. 21, the stress–strain curves of all the paints at rates of approximately 6000 s^{-1} and temperature of 20°C were compared. It shows that Coating D system which is made of Coatings A_1, B and C has a behaviour very similar to the Coating C although the initial elastic modulus is the same as that of Coating B. Coating A_3 behaves as Coating B with stress levels as low as half those encountered in Coatings A_2 and A_1.

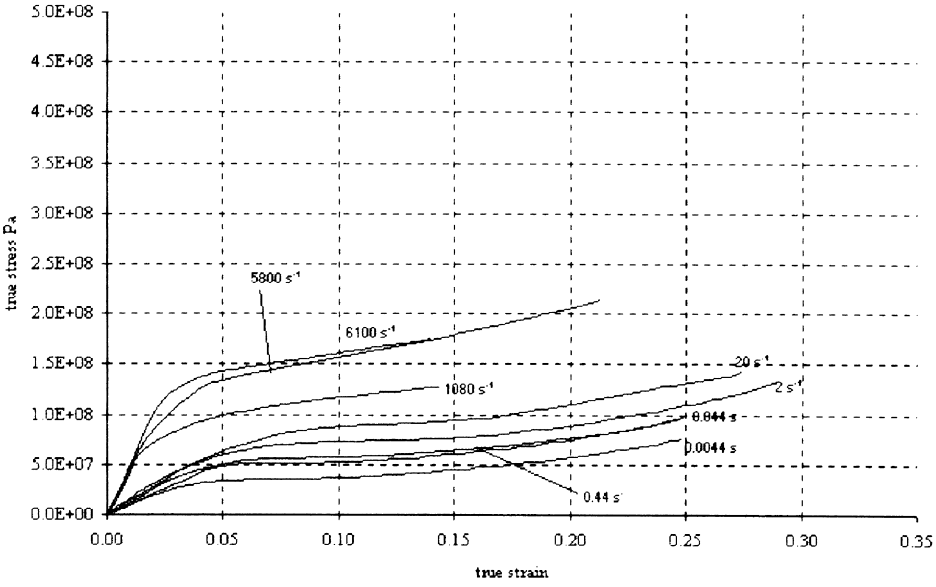

Fig. 17. Coating D: True stress–strain variation with strain rate at 20°C.

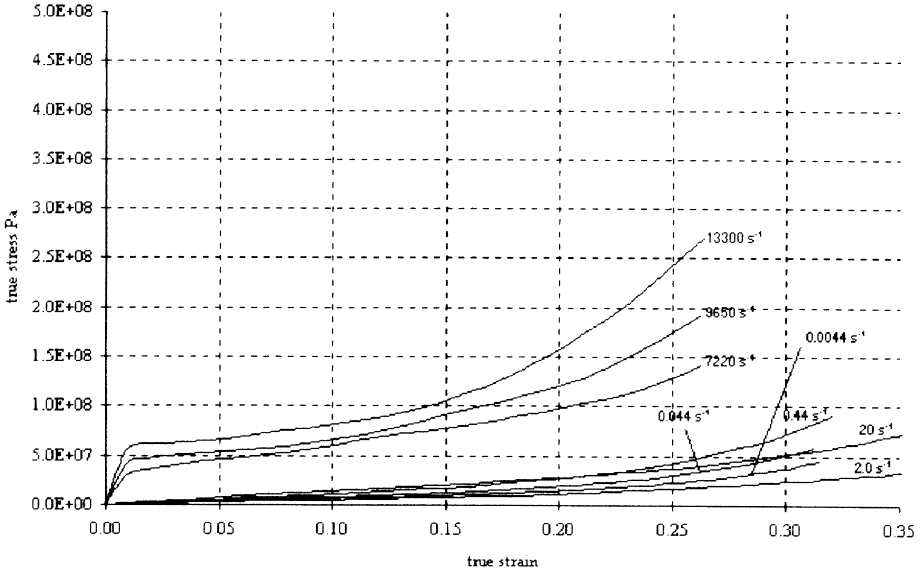

Fig. 18. Coating A_3: True stress–strain variation with strain rate at 40°C.

4.2. Variation of yield stress with strain rate and temperature

4.2.1. Eyring behaviour in polymers

Yielding in polymers has been described as a type of viscous flow, and the theory derived by Eyring for viscous flow in liquids has been applied to the behaviour of glassy polymers. To understand how this is done, the movement of polymer chain segments has to be considered. For a flow to occur the polymer segments have to move to an adjacent site and subsequently they have to overcome a potential energy barrier which is created by the presence of adjacent molecular segments. Consider the height of a potential barrier given by ΔH (known as the activation energy) and frequency of oscillation ν_0. It is thought to obey an Arrhenius type equation as follows [5]:

$$\nu_0 = B \exp\left(\frac{-\Delta H}{\mathrm{k}T}\right)$$

where B = temperature independent constant and k = Boltzmann′s constant.

If a shear stress is applied to the polymer, the rate of the segment jump over the potential barrier is increased. Hence, the height of the energy barrier to be overcome for flow is

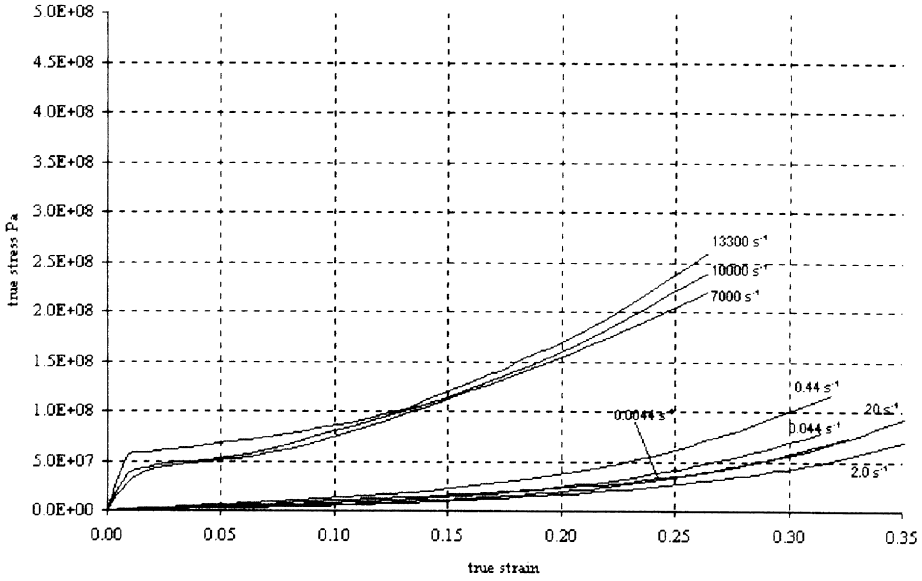

Fig. 19. Coating B: True stress–strain variation with strain rate at 40°C.

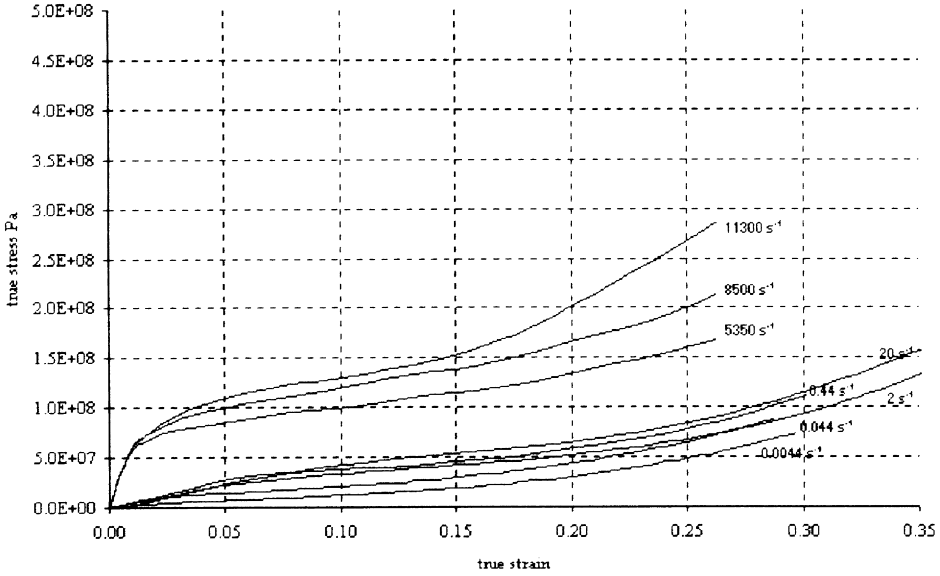

Fig. 20. Coating D: True stress–strain variation with strain rate at 40°C.

decreased by an amount $\frac{1}{2}\sigma Ax$ which is the work done in moving a segment by a distance x (A is the lattice cross-sectional area).

The frequency of forward motion is given by

$$\nu_f = \nu_0 \exp\left(\frac{\sigma Ax}{2kT}\right)$$

and the frequency of backward motion is given by

$$\nu_b = \nu_0 \exp\left(-\frac{\sigma Ax}{2kT}\right)$$

The resultant strain rate $\dot{\varepsilon}$ of the polymer segment is proportional to the difference between the frequency of forward and backward motion, i.e.

$$\dot{\varepsilon} = (\nu_f - \nu_b) = \nu_0 \exp\left(\frac{\sigma Ax}{2kT}\right) - \nu_0 \exp\left(-\frac{\sigma Ax}{2kT}\right)$$

where $v = Ax$ is the activation volume or 'Eyring volume' which is the volume of polymer segment that must move to cause flow or plastic deformation. Hence

$$\sigma_y = \frac{kT}{v}\left(\ln \dot{\varepsilon} - \ln \dot{\varepsilon}_0 + \frac{\Delta H}{kT}\right) \quad (5)$$

where $\dot{\varepsilon}_0$ is a constant pre-exponential factor. Therefore, a linear relationship is obtained between the yield stress and the logarithm of strain rate at a specific temperature T.

Some materials (polymethyl methacrylate, polyvinyl

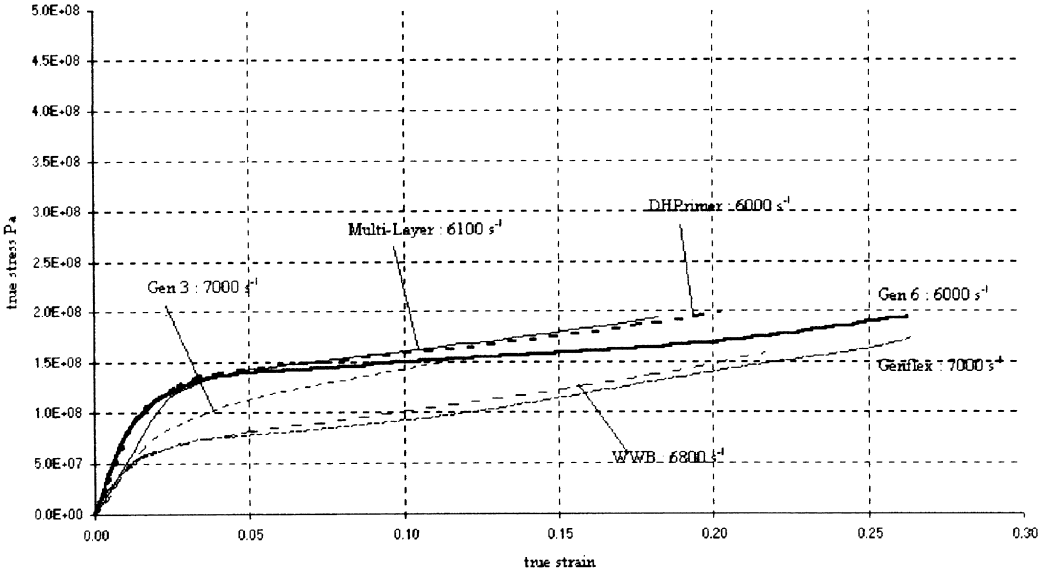

Fig. 21. Comparison between materials at high rates.

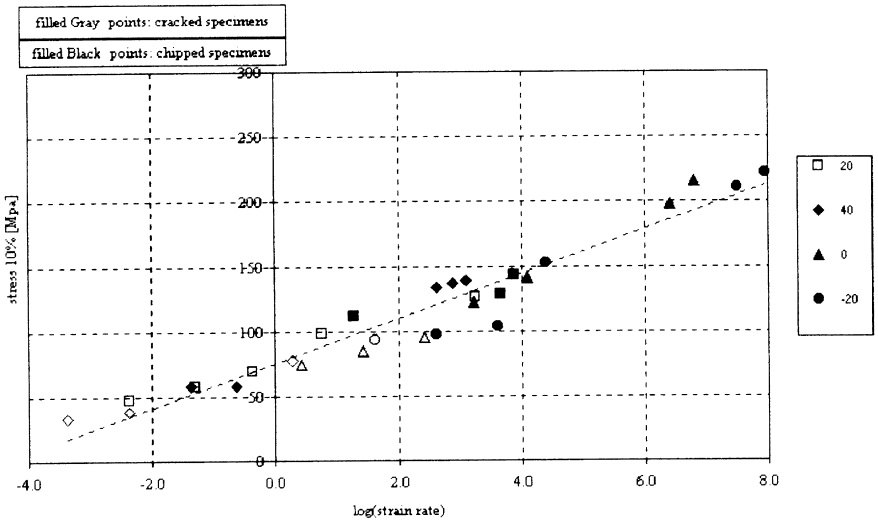

Fig. 22. Coating A_1: Strain rate–temperature plot for 10% flow stress.

chloride and polycarbonate) have shown a yield stress dependence on strain rate which increases more rapidly with higher strain rate and lower temperature [7]. Therefore, a modified Eyring equation has been proposed which is based on the assumption that more than one activated rate process exists with each flow unit in each process moving at the same strain rate but giving stresses that can be added together to give the total stress. For a two-rate process, the following equation has been derived from the original Eyring equation [8].

$$\frac{\sigma_y}{T} = \frac{k}{v_1}\left(\ln \dot{\varepsilon} - \ln \frac{\dot{\varepsilon}_{01}}{2} + \frac{\Delta H_1}{kT}\right) + \frac{k}{v_2} \sinh^{-1}\left[\frac{\dot{\varepsilon}}{\dot{\varepsilon}_{02}} \exp\left(\frac{\Delta H_1}{kT}\right)\right] \quad (6)$$

where $\sigma_y = \sigma_1 + \sigma_2$, σ_1 = flow σ associated with activation process 1 and σ_2 = flow σ associated with activation process 2.

At high temperatures and low strain rates, process 1 pre-dominates. Process 2 becomes important at low temperatures and high strain rates, and in this case, the inverse sinh term can be simplified to a simple inverse exponential term (as for process 1) to give an equation of the same form as Eq. (5) and given by Eq. (7). In general, however, it is kept as an inverse sinh term to incorporate an intermediate rate region where process 2 starts to influence process 1. The constants v_1, v_2, ΔH_1, ΔH_2, $\dot{\varepsilon}_{01}$ and $\dot{\varepsilon}_{02}$ can be calculated by considering the two extreme cases of low rate, high temperature and high rate, low temperature, because in these regions, there are no inverse sinh term and all relationships are linear.

$$\frac{\sigma_y}{T} = \frac{k}{v_1}\left(\ln \dot{\varepsilon} - \ln \frac{\dot{\varepsilon}_{01}}{2} + \frac{\Delta H_1}{kT}\right) + \frac{k}{v_2}\left(\ln \dot{\varepsilon} - \ln \frac{\dot{\varepsilon}_{01}}{2} + \frac{\Delta H_1}{kT}\right) \quad (7)$$

(a) At high temperature and/or low rate, process 1 predominates:

At constant rate $\dot{\varepsilon}$

$$\left(\frac{\partial \sigma_y}{\partial T}\right)\dot{\varepsilon} = \frac{k}{v_1}\left(\ln \dot{\varepsilon} - \ln \frac{\dot{\varepsilon}_{01}}{2}\right)$$

At constant temperature T

$$\left(\frac{\partial \sigma_y}{\partial \ln \dot{\varepsilon}}\right)T = \frac{kT}{v_1}$$

The intercept B_T is given by

$$B_T = \frac{kT}{v_1} \ln \frac{\dot{\varepsilon}_{01}}{2} + \frac{\Delta H_1}{v_1}$$

Hence, v_1, ΔH_1 and $\dot{\varepsilon}_{01}$ can be found if $(\partial \sigma_y/\partial T)\dot{\varepsilon}$, $(\partial \sigma_y/\partial \ln \dot{\varepsilon})T$ and B_T are known.

(b) At low temperature and/or high rate, process 1 and 2 combine:

At constant rate $\dot{\varepsilon}$

$$\left(\frac{\partial \sigma_y}{\partial T}\right)\dot{\varepsilon} = \frac{k}{v_1}\left(\ln \dot{\varepsilon} - \ln \frac{\dot{\varepsilon}_{01}}{2}\right) + \frac{k}{v_2}\left(\ln \dot{\varepsilon} - \ln \frac{\dot{\varepsilon}_{02}}{2}\right)$$

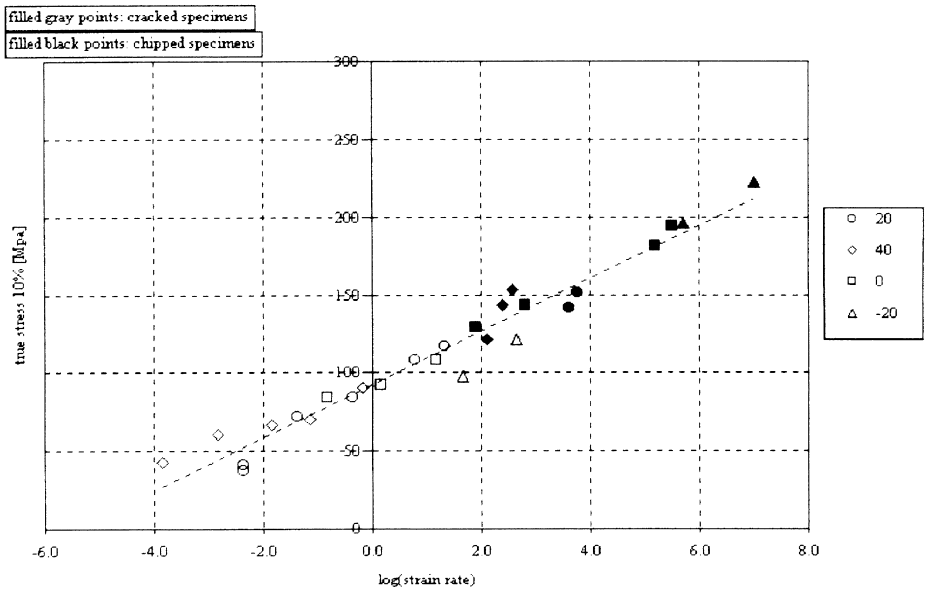

Fig. 23. Coating A_2: Strain rate–temperature plot for 10% flow stress.

At constant temperature T

$$\left(\frac{\partial \sigma_y}{\partial \ln \dot{\varepsilon}}\right)T = \frac{kT}{v_1} + \frac{kT}{v_2}$$

The intercept B_T is given by

$$B_T = -\frac{kT}{v_1} \ln \frac{\dot{\varepsilon}_{01}}{2} + \frac{\Delta H_1}{v_1} - \frac{kT}{v_2} \ln \frac{\dot{\varepsilon}_{02}}{2} + \frac{\Delta H_2}{v_2}$$

Hence, v_2, ΔH_2 and $\dot{\varepsilon}_{02}$ can be found if $(\partial \sigma_y/\partial T)\dot{\varepsilon}$, $(\partial \sigma_y/\partial \ln \dot{\varepsilon})T$ and B_T are known.

Therefore, plots of σ_y against T (at constant $\dot{\varepsilon}$) and plots of σ_y against $\ln\dot{\varepsilon}$ (at constant T) at each of these two regimes should give linear relationships that will enable v_1, ΔH_1, $\dot{\varepsilon}_{01}$, v_2, ΔH_2 and $\dot{\varepsilon}_{02}$ to be calculated.

4.2.2. Temperature shift factor to combine different temperatures

A plot of yield or 10% flow stress versus strain rate gives different parallel curves for lines at different temperatures. In an attempt to combine these curves into one master curve, a shift factor in terms of temperature [6] was used.

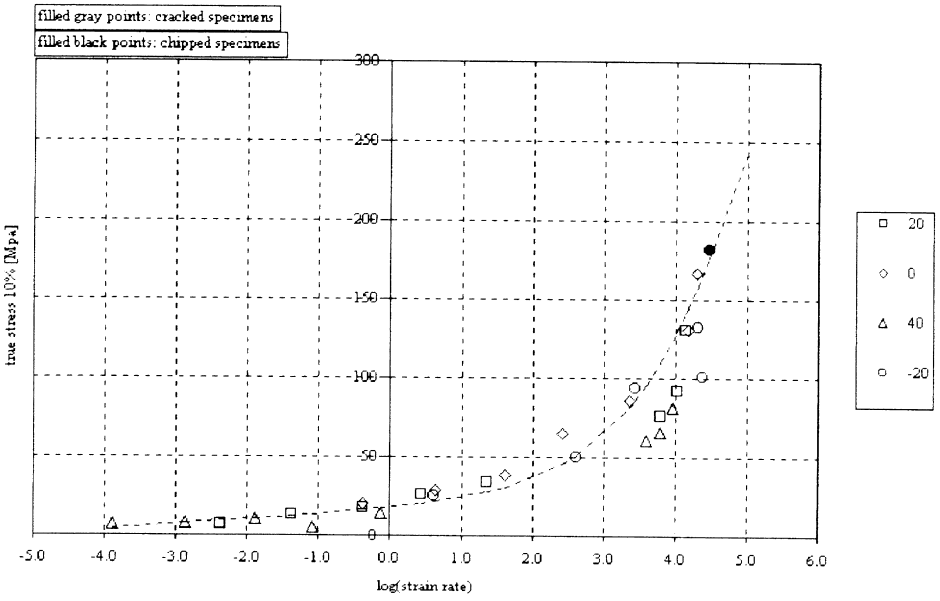

Fig. 24. Coating A_3: Strain rate–temperature plot for 10% flow stress.

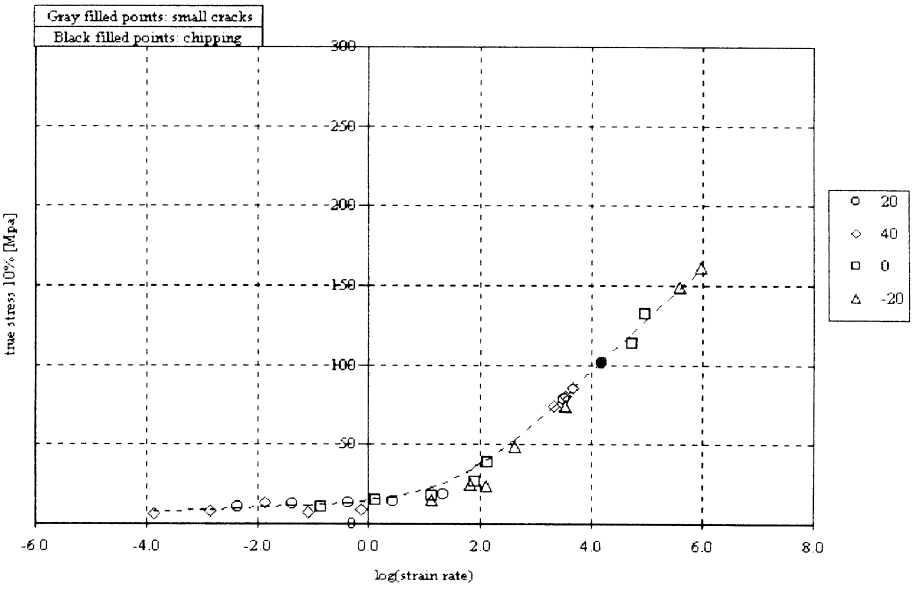

Fig. 25. Coating B: Strain rate–temperature plot for 10% flow stress.

4.2.3. Shifted Eyring plots at 20°C

The plots of the 10% flow stress (since the exact position of the yield stress could not be determined from most curves) are shown in Figs. 22–27.

While Coatings A_1, A_2 and C show a linear Eyring type behaviour with an average error of 7.4, 10.8 and 10.3 MPa, respectively, Coatings B, D and A_3 show a two-process Eyring type behaviour with the transition at approximately 10^2, 3.1×10^3 and 3×10^2 s^{-1} and average errors of 2.5 (low-intermediate rate), 2.3 (high rate) 7.5 (low-intermediate rate), 10.0 (high rate), and 3.5 (low-intermediate rate), 11.0 MPa (high rate), respectively. In Section 4.1.2, where strain softening was pointed out for Coatings B, D and A_3 at 40°C; it is now possible to see that this can be correlated to the fact that these materials show a two-process Eyring behaviour. A possible explanation could be that at intermediate strain rates, the first activation process (slow increase of yield stress with strain rate) is still dominant (referring to Figs. 24, 25 and 27). Hence, the strain rate softening effect on stress due to adiabatic heating which becomes apparent at intermediate strain rates (2.0, 20 s^{-1} from Figs. 15, 18–20) can overtake the stress hardening behaviour and cause a decrease in the stress with strain rate. However, as the strain rate increases further, the second

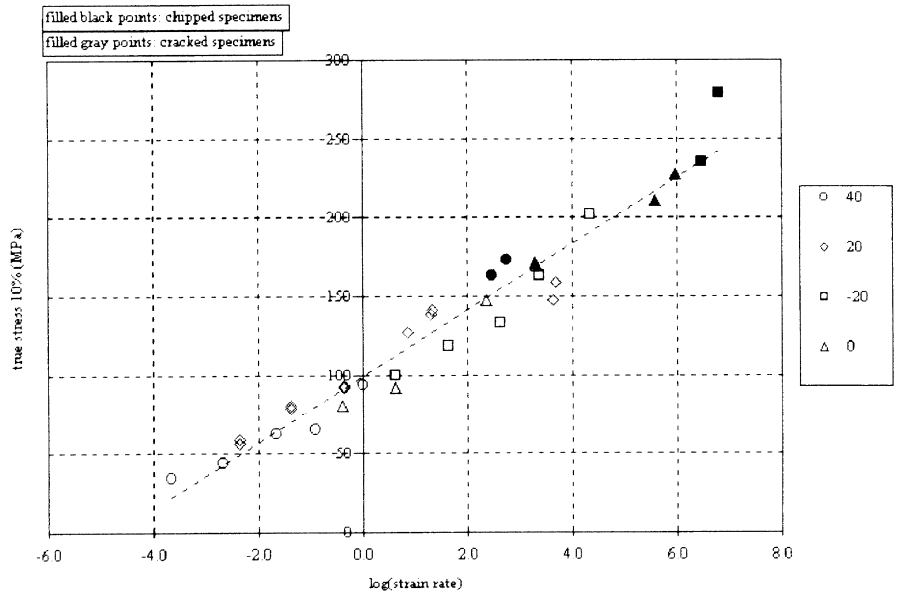

Fig. 26. Coating C: Strain rate–temperature plot for 10% flow stress.

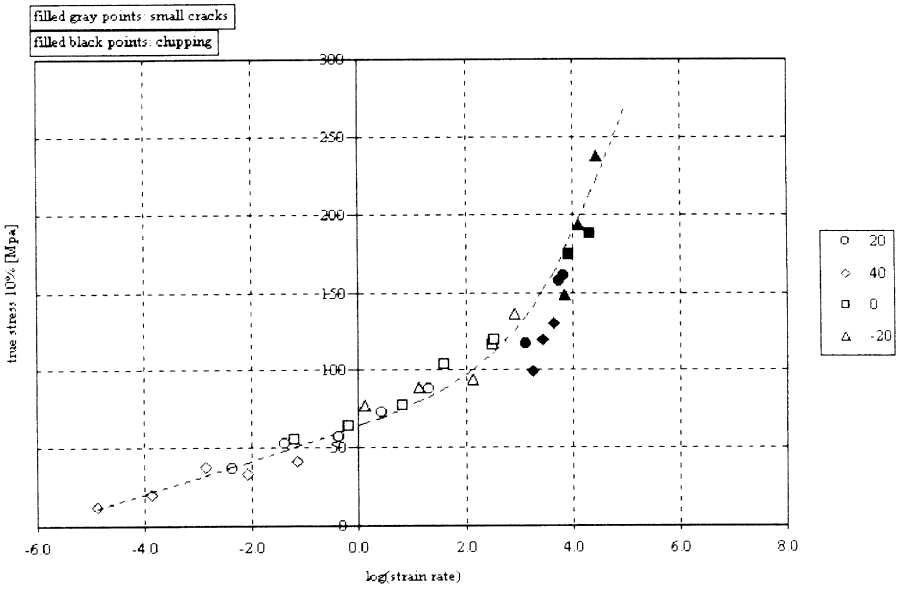

Fig. 27. Coating D: strain rate–temperature plot for 10% flow stress.

activation process becomes active; since it gives a much faster increase of yield stress with strain rate, it overtakes the net softening effect and stress hardening with strain rate is restored.

The method described in Section 4.2.1 is used to estimate the values of the activation energy ΔH, the activation volume v and the pre-exponential constant factor ε_0 for each material and each Eyring process and the values obtained are given in Table 1. For the cases of two Eyring processes, the variation of 10% flow stress with temperature at specific strain rates (low and high) was also plotted and the calculated gradients used. The fitted Eyring equation from these values is shown as a dotted line in Figs. 22–26.

The use of a shift factor enables a prediction of the behaviour of the material for strain rates of up to 10^6–$10^7\ s^{-1}$ for which experimental data is not available.

4.3. Empirical mapping of failure

In order to know if the onset of failure in the paint specimens could be related to a certain threshold strain rate, the strain rate–temperature plots included a record of points which cracked, chipped or suffered no failure as shown in Fig. 28. A cracked specimen represents one where radial or circumferential cracks spread through the specimen without causing any parts to separate from each other, while chipping is the state where the specimen was split into two or more bits.

Indeed, from the strain rate–temperature plots of Figs. 22–27 for all the paints, separate regions can be indentified which group these three modes belong. Hence, Table 2 gives values of approximate threshold strain rates for the onset of cracking and chipping for each paint material at 20°C.

Material D [made of A_1, B and C] gives a threshold rate of chipping which is slightly better than Coating C, lower than Coating B and much better than Coating A_1 by a factor of 10^4. Furthermore, A_1 is the worst clearcoat in terms of chipping, A_2 is better by a factor of 10^3 and A_3 is the best, by a factor of 10^5 over A_1.

5. Conclusion

In this paper, stress–strain data for automotive paints at strain rates ranging from 10^{-3} to $10^4\ s^{-1}$ and temperatures of −20 to 40°C have been presented and compared in terms of strain hardening behaviour and general stress levels. A

Table 1
Constant values for activation processes in paints

Materials	$\Delta H_1(J)$	$v_1(\text{Å}^3)$	$\ln \dot{\varepsilon}_{01}$	ΔH_2(J)	$v_2(\text{Å}^3)$	$\ln \dot{\varepsilon}_{02}$
A_1	1.27×10^{-19}	235.5	26.9	–	–	–
A_2	1.26×10^{-19}	237.8	25.6	–	–	–
A_3	3.19×10^{-19}	1391.8	73.4	2.76×10^{-20}	23.6	10.4
B	3.87×10^{-19}	4670.1	82.5	9.65×10^{-20}	125.6	25.4
C	1.24×10^{-19}	191.2	25.9	–	–	–
D	1.32×10^{-19}	385.1	26.6	2.82×10^{-20}	50.0	10.1

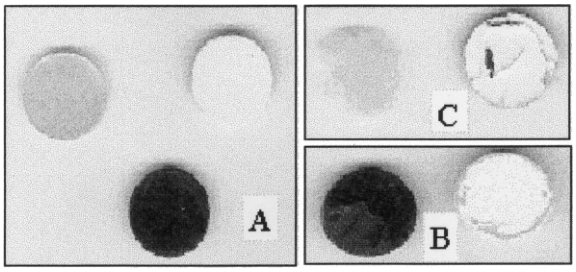

Fig. 28. (A) No failure; (B) cracks; and (C) chipped.

Table 2
Strain rate threshold for cracking and chipping at 20°C

Paint material	Strain rate cracking onset (s^{-1})	Strain rate chipping onset (s^{-1})
A_1	5.0×10^{-3}	10^{-1}
A_2	10	10^{2}
A_3	10^{4}	3.1×10^{4}
B	3.2×10^{3}	1.6×10^{4}
C	3.1	3.2×10^{2}
D	10^{-1}	10^{3}

general increase of stress with increasing strain rate and decreasing temperature was noted except for Coatings B at 20 and 40°C, Coating A_3 and Coating D at 40°C which showed a strain softening behaviour at medium rates. By plotting the 10% flow stress against the logarithm of strain rate and combining the data at different temperatures using a shift factor, the data was compared with the Eyring theory of yield. This showed that Coatings A_1, A_2 and C have one-process Eyring behaviour while Coatings A_3, B and D follow two-process behaviour for which the values of activation energies and volumes have been calculated. Furthermore, these plots enabled a mapping of safe and unsafe regions in terms of cracking and chipping (paint specimens split in pieces) and the strain rate thesholds for these regions were identified at room temperature. The stress–strain data model can now be used in a numerical model and the ultimate aim of which would be to determine the onset of delamination or growth of cracks from stress concentrations when a stone impacts the automotive multi-layer system. The empirical mapping of failure could be used as a bridge between the final aim and the available stress analysis numerical model for an understanding of how the unsafe regions in the paints progress on impact.

Acknowledgements

The authors would like to thank DuPont de Nemours Automotive Paints for their support of their work.

References

[1] Dioh NN. High strain rate behaviour of polymers at various temperatures. London: Mechanical Engineering, Imperial College, 1993.
[2] Dioh NN, Williams JG. The impact behaviour of paints. J Mat Sci 1994;29:6091–6.
[3] Kolsky H. Stress waves in solids. New York: Dover, 1963.
[4] Hamdan S, Swallowe GM. The strain-rate and temperature dependence of the mechanical properties of polyetherketone and polyetheretherketone. J Mat Sci 1996;31:1415–23.
[5] Young RJ. Introduction to polymers. London: Chapman and Hall, 1981.
[6] Ferry JD. Viscoelastic properties of polymers. New York: Wiley, 1970.
[7] Truss RW. Yield behaviour of linear polyethylene. J Pol Sci 1984;22:191.
[8] Ward IM. Mechanical properties of solid polymers. New York: Wiley, 1971.